Simulating dust grain-radiation coupling on a moving mesh

Ryan McKinnon,[1] Rahul Kannan,[2][*] Mark Vogelsberger,[1] Stephanie O'Neil,[1] Paul Torrey,[3] and Hui Li[1]

[1]*Department of Physics and Kavli Institute for Astrophysics and Space Research, Massachusetts Institute of Technology, Cambridge, MA 02139, USA*
[2]*Center for Astrophysics | Harvard & Smithsonian, Cambridge, MA 02138, USA*
[3]*Department of Astronomy, University of Florida, Gainesville, FL 32611, USA*

ABSTRACT

We present a model for the interaction between dust and radiation fields in the radiation hydrodynamic code AREPO-RT, which solves the moment-based radiative transfer equations on an unstructured moving mesh. Dust is directly treated using live simulation particles, each of which represent a population of grains that are coupled to hydrodynamic motion through a drag force. We introduce methods to calculate radiation pressure on and photon absorption by dust grains. By including a direct treatment of dust, we are able to calculate dust opacities and update radiation fields self-consistently based on the local dust distribution. This hybrid scheme coupling dust particles to an unstructured mesh for radiation is validated using several test problems with known analytic solutions, including dust driven via spherically-symmetric flux from a constant luminosity source and photon absorption from radiation incident on a thin layer of dust. Our methods are compatible with the multifrequency scheme in AREPO-RT, which treats UV and optical photons as single-scattered and IR photons as multi-scattered. At IR wavelengths, we model heating of and thermal emission from dust. Dust and gas are not assumed to be in local thermodynamic equilibrium but transfer energy through collisional exchange. We estimate dust temperatures by balancing these dust-radiation and dust-gas energy exchange rates. This framework for coupling dust and radiation can be applied in future radiation hydrodynamic simulations of galaxy formation.

Key words: methods: numerical – dust, extinction – galaxies: ISM – radiative transfer.

1 INTRODUCTION

In the interstellar medium, dust grains and radiation fields affect one another. Grains driven by radiation pressure can transfer momentum to nearby gas, helping to regulate star formation and launch galactic outflows (Krumholz & Matzner 2009; Murray, Quataert & Thompson 2010; Hopkins, Quataert & Murray 2012). Dust scatters and absorbs starlight and emits in the infrared (IR; Schlegel, Finkbeiner & Davis 1998; Bernstein, Freedman & Madore 2002; Schlafly & Finkbeiner 2011), influencing galactic spectral energy distributions (Silva et al. 1998; Dale et al. 2001). The temperatures of dust grains are affected by radiative heating, thermal emission, and collisional energy exchange with gas (Hollenbach & McKee 1979; Dwek 1986; Boulanger & Perault 1988), and small grains in particular are susceptible to non-equilibrium temperature fluctuations (Dwek 1986; Guhathakurta & Draine 1989; Siebenmorgen, Kruegel & Mathis 1992). Galaxy formation models must consider these physical processes when accounting for the impact of dust and radiation.

Owing to the computational cost, many works do not directly treat dust or radiation. Instead, they attempt to capture the effects of radiation pressure on dust grains through physically-motivated subgrid methods (Murray, Quataert & Thompson 2005; Hopkins, Quataert & Murray 2011; Agertz et al. 2013). This typically involves injecting momentum or thermal energy in gas surrounding sources of radiation like stars, avoiding the need to evolve radiation fields. For example, to mimic the impact of radiation multi-scattered by dust, momentum injection rates can increase as a function of local IR optical depth. Such radiation pressure feedback models have been used in cosmological settings and can reduce star formation (Aumer et al. 2013; Hopkins et al. 2014; Roškar et al. 2014; Agertz & Kravtsov 2015). To improve the accuracy of these subgrid radiation pressure models, there have been renewed efforts to develop numerical methods suited for simulations with limited resolution (Krumholz 2018; Hopkins & Grudić 2019).

In recent years, a variety of methods have been developed to more directly model radiation and its effect on dust. For example, Monte Carlo methods track the emission and absorption of individual photon packets but can be computationally expensive to run (e.g. Bjorkman & Wood 2001; Oxley & Woolfson 2003; Camps &

Baes 2015; Tsang & Milosavljević 2015; Smith et al. 2019). Other methods use long-characteristic ray tracing to solve the exact radiative transfer equation (e.g. Abel, Norman & Madau 1999; Abel & Wandelt 2002; Wise et al. 2012; Greif 2014; Jaura et al. 2018), although this can scale unfavourably with the number of sources. Alternatively, some mesh-based radiation hydrodynamics solvers combine moments of the radiative transfer equation with the M1 closure relation (Levermore 1984; Dubroca & Feugeas 1999), in which the Eddington tensor is calculated strictly from local quantities and is independent of the number of sources. Various codes employ the M1 closure (González, Audit & Huynh 2007; Rosdahl et al. 2013; Rosdahl & Teyssier 2015; Kannan et al. 2019b) and have been used in radiation hydrodynamic simulations of isolated disc galaxies (Rosdahl et al. 2015; Kannan et al. 2019a), quasar outflows via radiation pressure (Bieri et al. 2017; Costa et al. 2018b; Barnes et al. 2018), and reionisation calculations (see for eg. Rosdahl et al. 2018; Wu et al. 2019a,b).

In this work, we evolve radiation using the radiation hydrodynamics solver AREPO-RT (Kannan et al. 2019b) integrated into the unstructured moving-mesh code AREPO (Springel 2010). Kannan et al. (2019b) includes a simplified model for radiation pressure on, photon absorption by, and IR emission from dust grains, treating dust as a passive scalar perfectly coupled to hydrodynamic motion and in local thermodynamic equilibrium with gas. In this work, we relax those assumptions and adopt a more general treatment of dust in the context of radiation hydrodynamics. We do not treat dust as an element of gas cells but instead using simulation particles (McKinnon et al. 2018). This approach allows richer and more realistic dynamical and thermal interactions among dust, gas, and radiation. We present our methods and test problems in Section 2 and conclude in Section 4.

2   METHODS

We start with a brief summary of the equation of motions for dust and gas components coupled through aerodynamic drag and possibly subject to external accelerations. We refer the reader to Section 2 in McKinnon et al. (2018) for background details. A dust grain of mass m_d feels an acceleration

$$\frac{d\mathbf{v}_d}{dt} = -\frac{K_s(\mathbf{v}_d - \mathbf{v}_g)}{m_d} + \mathbf{a}_{d,\text{ext}}, \tag{1}$$

where $\mathbf{v}_d$ and $\mathbf{v}_g$ are the local dust and gas velocities, respectively, $\mathbf{a}_{d,\text{ext}}$ accounts for additional sources of dust acceleration (e.g. gravity or radiation pressure), and K_s is a drag coefficient. Similarly, the gas acceleration is given by

$$\frac{d\mathbf{v}_g}{dt} = -\frac{\nabla P}{\rho_g} + \frac{\rho_d K_s(\mathbf{v}_d - \mathbf{v}_g)}{\rho_g m_d} + \mathbf{a}_{g,\text{ext}}, \tag{2}$$

where P denotes gas pressure, ρ_d and ρ_g are the dust and gas density, respectively, and $\mathbf{a}_{g,\text{ext}}$ is the external gas acceleration. For use later, we define the dust-to-gas ratio $D \equiv \rho_d/\rho_g$. Here, the drag backreaction force by dust on gas is exactly opposite to the drag force by gas on dust. For drag in the Epstein regime, the equations of motion can be rewritten in terms of $t_s \equiv m_d/[K_s(1+D)]$, the stopping time-scale for drag, whose value is given by the approximation

$$t_s = \frac{\sqrt{\pi\gamma}a\rho_{gr}}{2\sqrt{2}\rho c_s}\left(1 + \frac{9\pi}{128}\left|\frac{\mathbf{v}_d - \mathbf{v}_g}{c_s}\right|^2\right)^{-1/2}, \tag{3}$$

for a given grain size a, internal solid density of dust grains ρ_{gr}, total density $\rho \equiv \rho_g + \rho_d$, and gas sound speed c_s (Paardekooper

& Mellema 2006; Price et al. 2017). The dust-to-gas ratio D affects the backreaction of dust dragging gas: when $D \ll 1$, the gas drag acceleration is significantly smaller than the dust acceleration. Since $D \approx 0.01$ for the Milky Way and other nearby galaxies (e.g. Draine et al. 2007), in galaxy simulations it is often reasonable to neglect the backreaction of drag on gas.

However, dust dynamics are applicable in a wide variety of settings, and it is worthwhile to relax the assumption of low dust-to-gas ratio. Below, we extend the drag implementation of McKinnon et al. (2018), which neglected drag backreaction on gas, to handle drag coupling at arbitrary dust-to-gas ratio. We adopt the second-order semi-implicit time integrator presented in Lorén-Aguilar & Bate (2015). Defining the functions

$$\xi(\Delta t) = \frac{1 - e^{-\Delta t/t_s}}{1 + D} \tag{4}$$

and

$$\Lambda(\Delta t) = (\Delta t + t_s)\xi(\Delta t) - \frac{\Delta t}{1 + D}, \tag{5}$$

the velocity update of a dust particle from time t to $t + \Delta t$ is given by

$$\begin{aligned}\mathbf{v}_d(t + \Delta t) = \tilde{\mathbf{v}}_d(t + \Delta t) &- \xi(\Delta t)\left[\tilde{\mathbf{v}}_d(t + \Delta t) - \tilde{\mathbf{v}}_g(t + \Delta t)\right] \\ &+ \Lambda(\Delta t)\left[\mathbf{a}_{d,\text{ext}}(t) - \mathbf{a}_{g,\text{ext}}(t) + \frac{\nabla P}{\rho_g}\right],\end{aligned} \tag{6}$$

where $\mathbf{v}_d(t + \Delta t)$ is the dust particle velocity after the drag update and $\tilde{\mathbf{v}}_d(t + \Delta t)$ and $\tilde{\mathbf{v}}_g(t + \Delta t)$ are the dust and gas velocities at time $t + \Delta t$ after accounting for non-drag accelerations. We apply equation (6) in the following SPH-like fashion to conserve total momentum. After calculating the change in a dust particle's momentum $\Delta\mathbf{p}_d$, we subtract momentum $w_i\Delta\mathbf{p}_d$ from each of the N_{ngb} closest gas cells, where w_i is a weight assigned to cell i in this set. The amount of momentum change in each neighboring gas cell is kernel-weighted so that closer gas cells lose a greater fraction of $\Delta\mathbf{p}_d$. In our work, we adopt the standard cubic spline kernel.

The dissipation of total dust and gas kinetic energy from drag leads to frictional heating of the gas (e.g. Laibe & Price 2012). When applying equation (6), we calculate the change in kinetic energy of the dust particle ΔK_d. Then, after updating the momentum of local gas cell i, we determine its change in kinetic energy ΔK_g. The internal energy of the cell is then increased by $-(w_i\Delta K_d + \Delta K_g)$. Summing over all cells about a dust particle, the gas internal energy increases by the amount total dust and gas kinetic energy decreases.

2.1   Interaction between dust grains and radiation

Gravity and drag are not the only dynamical forces that act on interstellar dust grains. Since dust provides a source of opacity to radiation, the resulting radiation pressure force (e.g. Weingartner & Draine 2001) can also affect dust and gas dynamics. This has potential implications for the efficiency of stellar feedback and galactic outflows. For example, some models predict that multi-scattering of IR radiation due to dust opacity can enhance self-regulation of star formation (Murray, Quataert & Thompson 2010; Hopkins, Quataert & Murray 2011; Agertz et al. 2013) and boost gas outflows in galaxies up to IR optical depths of $\tau_{\text{IR}} \approx 10$ (Thompson et al. 2015; Costa et al. 2018a). However, others suggest that dust reprocessing of radiation does not strongly affect wind momentum

flux (Krumholz & Thompson 2013; Reissl et al. 2018). The interaction between dust and radiation can also affect the CGM in addition to the ISM. Radiation pressure can efficiently drive dust grains into galactic haloes, with grains of different chemical composition feeling different strength forces (Ferrara et al. 1991). Given the reliance of galaxy formation simulations on feedback physics, it is natural to want to model the interaction between dust and radiation in a more direct manner.

Recently, Kannan et al. (2019b) developed radiation hydrodynamics methods for the moving-mesh code AREPO (Springel 2010), capable of tracking multifrequency radiation transport and thermochemistry. Here, we briefly summarise these methods and refer the reader to Sections 2 and 3 of Kannan et al. (2019b) for a more complete description. In general, radiative transfer is formulated in terms of specific intensity $I_\nu(\mathbf{x}, \mathbf{n}, t)$, which at position $\mathbf{x}$ and time t quantifies the rate of change of radiation energy at frequency ν per unit time, per unit area in the direction $\mathbf{n}$, per unit solid angle, and per unit frequency. This evolves according to the radiative transfer equation,

$$\frac{1}{\tilde{c}}\frac{\partial I_\nu}{\partial t} + \mathbf{n} \cdot \nabla I_\nu = j_\nu - \kappa_\nu \rho I_\nu, \tag{7}$$

where $\tilde{c}$ is the propagation speed of radiation, j_ν denotes the emission coefficient, κ_ν is the gas opacity, and ρ is the gas density. Numerically solving the radiative transfer equation is challenging, given the large number of variables. One approach is to take moments of the radiative transfer equation, yielding

$$\frac{\partial E}{\partial t} + \nabla \cdot \mathbf{F} = S - \kappa_E \rho \tilde{c} E \tag{8}$$

and

$$\frac{\partial F}{\partial t} + \tilde{c}^2 \nabla \cdot \mathbb{P} = -\kappa_F \rho \tilde{c} \mathbf{F}, \tag{9}$$

where S denotes the emission coefficient integrated over frequency and solid angle, κ_E and κ_F are the energy- and flux-weighted mean opacities, and the radiation energy density E, flux F, and pressure $\mathbb{P}$ are given by

$$\{\tilde{c}E, F, \mathbb{P}\} = \int_{\nu_1}^{\nu_2} \int_{4\pi} \{1, \mathbf{n}, \mathbf{n} \otimes \mathbf{n}\} I_\nu \, d\Omega \, d\nu. \tag{10}$$

All quantities are integrated over a frequency interval $[\nu_1, \nu_2]$. To simplify this system, AREPO-RT employs the M1 closure (Levermore 1984; Dubroca & Feugeas 1999) that calculates the pressure strictly in terms of the local radiation energy density and flux. This approximation yields a computational cost independent of the number of radiation sources. Equations (8) and (9) are solved on an unstructured moving mesh using an operator-split approach, breaking the moment equations into transport and source and sink terms. To calculate intercell fluxes, AREPO-RT employs a Harten-Lax-van Leer or global Lax-Friedrichs Riemann solver.

The propagation of radiation also affects hydrodynamics. The momentum conservation equation takes the form

$$\frac{\partial(\rho\mathbf{v})}{\partial t} + \nabla \cdot (\rho\mathbf{v} \otimes \mathbf{v} + P\mathbb{I}) = \frac{\kappa_F \rho F}{c}, \tag{11}$$

where $\mathbf{v}$ is the gas velocity, P is the thermal pressure, $\mathbb{I}$ is the identity tensor, and c is the speed of light. In Kannan et al. (2019b), the opacities entering the above equations are calculated for individual gas cells using crude approximations or a simplified dust model treating dust as a passive scalar perfectly coupled to hydrodynamic motion (McKinnon, Torrey & Vogelsberger 2016). In this work, we instead model dust using live simulation particles (McKinnon et al. 2018) and not as a property of gas cells. We describe below how

the methods in Kannan et al. (2019b) can be extended to model radiation pressure on and photon absorption by dust grains using this hybrid gas cell and dust particle scheme. As a result, dust opacities are calculated self-consistently using the local distribution of dust. We generalize these methods to multifrequency radiation and distributions of grain sizes and discuss how dust grains can exchange energy with IR radiation and gas.

2.1.1 Calculating radiation pressure on populations of grains

The methods described in McKinnon et al. (2018) model dust using simulation particles representing ensembles of grains of different sizes. Each particle has a grain size distribution, discretised into $N_{\rm GSD}$ grain size bins with different typical sizes. Similarly, the radiative transfer scheme introduced in Kannan et al. (2019b) solves for the propagation of radiation in $N_{\rm RT}$ different frequency bins (e.g. to model different UV wavelength ranges or simultaneous UV and IR radiation fields).

We calculate the radiation pressure force $\mathbf{f}_{\rm pr}$ on a dust particle with grains of different sizes in a kernel-smoothed manner, interpolating over $N_{\rm ngb}$ neighboring gas cells. In the general case of multifrequency, anisotropic radiation (Weingartner & Draine 2001), this radiation pressure force takes the form

$$\mathbf{f}_{\rm pr} = \sum_{k=0}^{N_{\rm ngb}-1} w_k \left[\sum_{i=0}^{N_{\rm GSD}-1} \sum_{j=0}^{N_{\rm RT}-1} \left(\frac{\mathbf{F_{j,k}}}{c} \right) N_i \pi a_i^{c\,2} Q_{\rm pr}(a_i^c, \lambda_j) \right], \tag{12}$$

where $\mathbf{F_{j,k}}$ and λ_j are the energy flux and (mean) wavelength in radiative transfer bin j for neighboring gas cell k, and N_i and a_i^c are the number of grains and midpoint of grain size bin i. We use the same cubic spline kernel as in McKinnon et al. (2018) to calculate the weight w_k for gas cell k as a function of its distance from the given dust particle. These weights are normalised such that they sum to unity over all neighboring gas cells. In equation (12), the term in brackets represents what the radiation pressure force would be if all grain cross section were concentrated in gas cell k, summing over all grain sizes and frequency bins.

This force depends on the radiation pressure efficiency $Q_{\rm pr}(a, \lambda)$, which is a dimensionless factor denoting the ratio of radiation pressure cross section to geometric cross section for a dust grain of size a and wavelength of incident radiation λ. This efficiency factor is defined as $Q_{\rm pr} \equiv Q_{\rm abs} + (1 - \langle\cos\theta\rangle)Q_{\rm sca}$, where $Q_{\rm abs}$ is the ratio of absorption cross section to geometric cross section, $Q_{\rm sca}$ is the ratio of scattering cross section to geometric cross section, $\langle\cos\theta\rangle$ is the average cosine of scattering angle θ, and all three quantities are functions of grain size and wavelength.

Following McKinnon et al. (2018), we use tabulated values of $Q_{\rm abs}$, $Q_{\rm sca}$, and $\langle\cos\theta\rangle$ for silicate and graphite grains from Draine & Lee (1984) and Laor & Draine (1993). These tabulations cover the grain size range $0.001\,\mu\rm m < a < 10\,\mu\rm m$ and wavelength range $0.001\,\mu\rm m < \lambda < 1000\,\mu\rm m$. We perform two-dimensional logarithmic interpolation to calculate $Q_{\rm pr}(a, \lambda)$ values at arbitrary grain size and wavelength, averaging results for silicate and graphite grains.

2.1.2 Absorption of photons from dust grain opacity

Dust grains absorb and reradiate in the IR a sizeable fraction of starlight, often estimated around 30 per cent (Soifer & Neugebauer 1991; Popescu & Tuffs 2002). We first describe absorption in the

single-scattering regime (e.g. for UV frequency bins, as in Section 3.2.1 of Kannan et al. 2019b).

We account for photon absorption in a kernel-smoothed fashion, by spreading a dust particle's absorption cross section among neighboring gas cells to update energy densities and fluxes. This approach effectively replaces the dust opacity terms in equations 47 and 48 in Kannan et al. (2019b) that are used in simulations lacking live dust particles. Specifically, when processing an active dust particle we update the energy density in radiation bin j for neighboring gas cell k according to the rate

$$\frac{\partial E_{j,k}}{\partial t} = -\frac{w_k \tilde{c} E_{j,k}}{V_k} \sum_{i=0}^{N_{\mathrm{GSD}}-1} N_i \pi a_i^{\mathrm{c}\,2} Q_{\mathrm{abs}}(a_i^{\mathrm{c}}, \lambda_j), \qquad (13)$$

where w_k is the gas cell's kernel weight, $\tilde{c}$ is the reduced speed of light, and V_k is the gas cell volume. As in equation (12), N_i is the number of grains in size bin i for the dust particle, a_i^{c} is the grain size at the midpoint of size bin i, and λ_j is the (mean) wavelength in radiation bin j. The absorption cross section efficiency Q_{abs}, described in Section 2.1.1, is a function of grain size and wavelength of radiation. Likewise, the flux in frequency bin j of gas cell k is updated using the rate

$$\frac{\partial \mathbf{F_{j,k}}}{\partial t} = -\frac{w_k \tilde{c} \mathbf{F_{j,k}}}{V_k} \sum_{i=0}^{N_{\mathrm{GSD}}-1} N_i \pi a_i^{\mathrm{c}\,2} Q_{\mathrm{abs}}(a_i^{\mathrm{c}}, \lambda_j). \qquad (14)$$

2.1.3 Multifrequency radiation and dust coupling

The radiation hydrodynamics methods in Kannan et al. (2019b) are capable of treating multifrequency radiation, divided into several UV and optical bins (e.g. corresponding to H I, He I, and He II ionisation) and one IR bin. Photons in UV and optical bins are "single-scattered": the energy absorbed by dust at these wavelengths is reemitted as IR radiation. On the other hand, IR photons are "multi-scattered": dust grains can absorb IR photons but also thermally emit in the IR.

In the notation below, we assume that the N_{RT} radiation bins are ordered by decreasing frequency, so that the IR bin is last. Then, the IR energy density in gas cell k, $E_{\mathrm{IR},k}$, changes according to

$$\frac{\partial E_{\mathrm{IR},k}}{\partial t} = \frac{\partial E_{\mathrm{IR},k}^{\mathrm{reprocess}}}{\partial t} + \frac{\partial E_{\mathrm{IR},k}^{\mathrm{thermal}}}{\partial t}, \qquad (15)$$

the sum of reprocessing rates (i.e. energy from UV and optical photons that is reemitted in the IR) and thermal dust exchange rates (i.e. dust emission and absorption of IR photons), respectively. In this section, we focus on reprocessing of UV and optical radiation and discuss thermal IR exchange next in Section 2.1.4. Then, the rate at which the IR energy density increases is given by the total rate at which UV and optical energy density decreases. That is,

$$\frac{\partial E_{\mathrm{IR},k}^{\mathrm{reprocess}}}{\partial t} = -\sum_{j=0}^{N_{\mathrm{RT}}-2} \frac{\partial E_{j,k}}{\partial t} \qquad (16)$$

where the sum is over all non-IR bins and the energy absorption rate in radiation bin j, $\partial E_{j,k}/\partial t$, is computed via equation (13). Additionally, paralleling equation (14), the IR flux in gas cell k evolves according to

$$\frac{\partial \mathbf{F_{IR,k}}}{\partial t} = -\frac{w_k \tilde{c} \mathbf{F_{IR,k}}}{V_k} \sum_{i=0}^{N_{\mathrm{GSD}}-1} N_i \pi a_i^{\mathrm{c}\,2} Q_{\mathrm{abs}}(a_i^{\mathrm{c}}, \lambda_{\mathrm{IR}}). \qquad (17)$$

2.1.4 Thermal coupling for infrared radiation

Dust grains both emit and absorb IR photons (Dwek 1986; Krumholz & Thompson 2013) and also collisionally exchange energy with gas (Hollenbach & McKee 1979; Omukai 2000; Goldsmith 2001). These competing processes affect the temperature of a population of dust grains (Goldsmith 2001; Krumholz 2014; Smith et al. 2017). Small grains in particular are susceptible to stochastic heating and temperature fluctuations (Guhathakurta & Draine 1989; Siebenmorgen, Kruegel & Mathis 1992; Draine & Li 2001), and methods to calculate and evolve dust temperature probability distributions are used in various applications (e.g. Pavlyuchenkov et al. 2012; Camps et al. 2015). However, given the limited resolution our simulations, we instead follow the approach in DESPOTIC (Krumholz 2014) and GRACKLE (Smith et al. 2017), treating dust grains as being in thermal equilibrium and neglecting such temperature fluctuations.

As with equation (13), we perform the coupling between dust, gas, and IR radiation in a kernel-smoothed manner, where dust particles exchange energy with their surrounding neighbors. Since dust particles are superpositions of grains of different sizes, we allow for the possibility that the dust temperature varies from one grain size bin to another. When considering the exchange between a dust particle and neighboring gas cell k, the IR radiation energy density $E_{\mathrm{IR},k}$, dust energy density u_{d}, and gas energy density $u_{\mathrm{g},k}$ evolve according to the system

$$\begin{aligned} \frac{\partial E_{\mathrm{IR},k}^{\mathrm{thermal}}}{\partial t} &= \Lambda_{\mathrm{dr},k} \\ \frac{\partial u_{\mathrm{d}}}{\partial t} &= -\Lambda_{\mathrm{dr},k} - \Lambda_{\mathrm{dg},k} \\ \frac{\partial u_{\mathrm{g},k}}{\partial t} &= \Lambda_{\mathrm{dg},k}. \end{aligned} \qquad (18)$$

Here, the dust-radiation energy exchange rate per unit volume (e.g. Krumholz & Thompson 2013) in gas cell k is given by $\Lambda_{\mathrm{dr},k} = \sum_{i=0}^{N_{\mathrm{GSD}}-1} \Lambda_{\mathrm{dr},k,i}$, where the contribution from grains in size bin i is

$$\Lambda_{\mathrm{dr},k,i} = \left[\frac{w_k}{V_k} N_i \pi a_i^{\mathrm{c}\,2} Q_{\mathrm{abs}}(a_i^{\mathrm{c}}, \lambda_{\mathrm{IR}}) \right] (c a_{\mathrm{B}} T_{\mathrm{d},k,i}^4 - \tilde{c} E_{\mathrm{IR},k}), \quad (19)$$

where w_k is the gas cell's kernel weight (see equation 12), V_k is the cell volume, a_{B} is the radiation constant, and $T_{\mathrm{d},k,i}$ is the cell's dust temperature for grains in size bin i. The prefactor in equation (19) is the cross section per unit volume in gas cell k, obtained by assigning a weighted fraction of the dust particle's grain population to the cell. Also, the dust-gas energy exchange rate per unit volume (e.g. Burke & Hollenbach 1983; Hollenbach & McKee 1989) is calculated via $\Lambda_{\mathrm{dg},k} = \sum_{i=0}^{N_{\mathrm{GSD}}-1} \Lambda_{\mathrm{dg},k,i}$, using the exchange rate with grains in size bin i of

$$\Lambda_{\mathrm{dg},k,i} = \left[\frac{w_k}{V_k} N_i \pi a_i^{\mathrm{c}\,2} \right] n_{\mathrm{H},k} v_{\mathrm{th},k} \overline{\alpha}_T (2 k_{\mathrm{B}}) (T_{\mathrm{d},k,i} - T_{\mathrm{g},k}). \quad (20)$$

Here, $n_{\mathrm{H},k}$ is the hydrogen number density in gas cell k, $\overline{\alpha}_T \approx 0.5$ is an estimated "accommodation coefficient" (see equation 9 in Burke & Hollenbach 1983), k_{B} is the Boltzmann constant, $T_{\mathrm{g},k}$ is the gas temperature, and

$$v_{\mathrm{th},k} \equiv \left(\frac{8 k_{\mathrm{B}} T_{\mathrm{g},k}}{\pi m_{\mathrm{p}}} \right)^{1/2} \qquad (21)$$

is the gas thermal velocity.

Since dust grains reach thermal equilibrium on a rapid timescale (Woitke 2006; Krumholz 2014; Smith et al. 2017), we calculate the dust temperature $T_{\mathrm{d},k,i}$ that grains in size bin i in gas
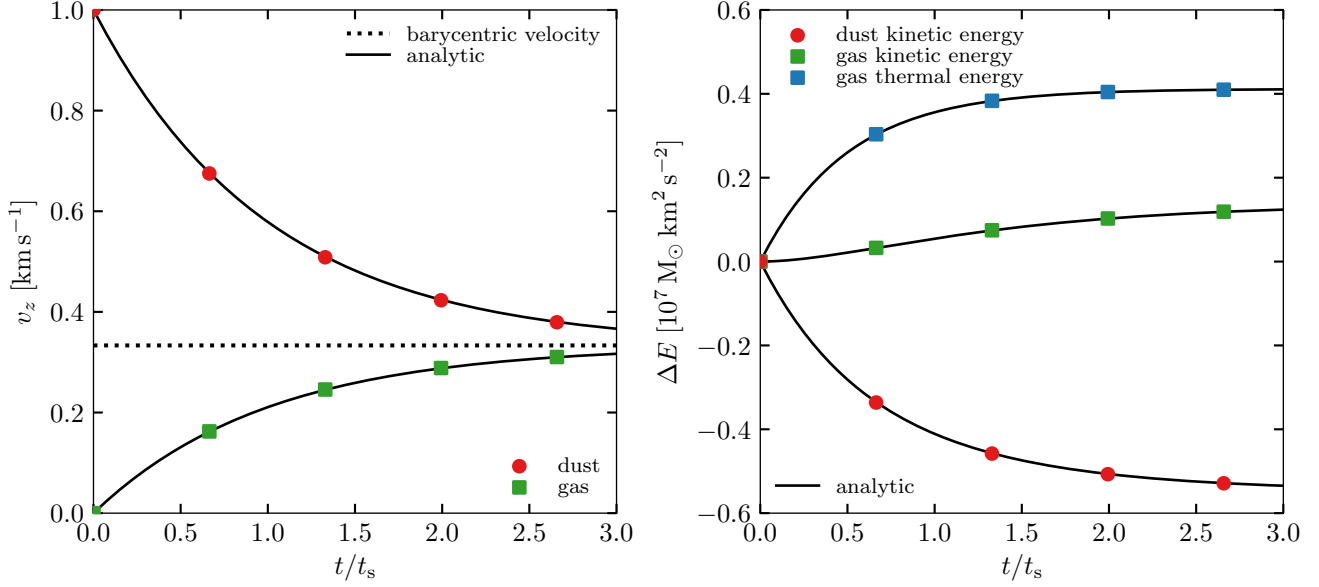
Figure 1. Left panel: velocity profiles versus time for a dust and gas mixture coupled via drag with an initial dust-to-gas ratio of $D = 0.5$. Coloured points show simulation results as the dust and gas velocities approach the barycentric velocity (dotted line), while the solid lines indicate the analytic predictions. Time is given in units of the drag stopping time-scale t_s. Right panel: change in different energy components versus time. Dust kinetic energy (red) decreases, while gas kinetic energy (green) increases. The net loss of kinetic energy from drag leads to an increase in gas thermal energy (blue).

cell k have by solving the instantaneous equilibrium condition $\Lambda_{\mathrm{dr},k,i}(T_{\mathrm{d},k,i}) + \Lambda_{\mathrm{dg},k,i}(T_{\mathrm{d},k,i}) = 0$ using Newton's method for root-finding. Using this dust temperature, over the dust particle's time-step Δt we then add $\Lambda_{\mathrm{dr},k,i} V_k \Delta t$ in IR radiation energy and $\Lambda_{\mathrm{dg},k,i} V_k \Delta t$ in thermal energy to gas cell k. This process is repeated for all grain size bins and all gas cells within a dust particle's smoothing length. An average dust temperature for size bin i in the dust particle can be calculated as $T_{\mathrm{d},i} = \sum_{k=0}^{N_{\mathrm{ngb}}-1} w_k T_{\mathrm{d},k,i}$.

3 TEST PROBLEMS

3.1 Demonstration of drag and kinetic energy dissipation

When the dust-to-gas ratio D is of order unity, drag impacts both dust and gas. To illustrate this in a simple test, we initialise a box of side length 1 kpc with 32^3 gas cells and 32^3 dust particles arranged on an equispaced lattice. Gas cell masses are set so that the box has a uniform gas density of $n = 1\,\mathrm{cm}^{-3}$. We adopt a dust-to-gas ratio of $D = 0.5$, so that the mass of a dust particle is half the mass of a gas cell. Initially, gas is at rest ($\mathbf{v}_{\mathrm{g}}(t = 0) = \mathbf{0}\,\mathrm{km\,s}^{-1}$), and dust is given nonzero velocity along the z axis ($\mathbf{v}_{\mathrm{d}}(t = 0) \equiv \mathbf{v}_0 = 1\,\mathrm{km\,s}^{-1}\,\hat{\mathbf{z}}$).

Dust particles are assumed to consist of $0.1\,\mu\mathrm{m}$ grains, and the internal energy per unit mass of the gas is initially $u = 1000\,\mathrm{km^2\,s^{-2}}$. From the values above, one can calculate the stopping time-scale t_s over which the drag force acts. In this test, the analytic prediction for gas velocity is

$$\mathbf{v}_{\mathrm{g}}(t) = \left(\frac{D}{1+D}\right)\left(1 - e^{-t/t_s}\right)\mathbf{v}_0, \tag{22}$$

and the analytic prediction for dust velocity is

$$\mathbf{v}_{\mathrm{d}}(t) = \left(\frac{1}{1+D}\right)\left(D + e^{-t/t_s}\right)\mathbf{v}_0. \tag{23}$$

As $t \to \infty$, both $\mathbf{v}_{\mathrm{g}}$ and $\mathbf{v}_{\mathrm{d}} \to D\mathbf{v}_0/(1 + D) = \mathbf{v}_0/3$, showing that gas and dust are expected to move at the barycentric velocity of the mixture.

Figure 1 shows the time evolution of dust and gas velocities and energies for this mixture coupled by drag. Since the drag force acts in an equal and opposite manner on dust and gas components and the dust-to-gas ratio is less than unity, dust velocities decrease more quickly than gas velocities increase. The initial relative velocity between dust and gas rapidly decays. After just two stopping time-scales, the dust and gas velocities are already within thirty per cent of the barycentric velocity. Over time, more dust kinetic energy is lost than gas kinetic energy is gained. The net dissipation of kinetic energy leads to an increase in gas thermal energy. In both panels of Figure 1, simulation results for velocity and energy evolution are visually indistinguishable from analytic predictions.

3.2 Spherically symmetric radiation pressure test problem

To demonstrate our radiation pressure scheme, we first consider a monochromatic radiation source with constant luminosity L and grains of a single fixed size a. Analytically, a dust grain at distance r from the radiation source feels a radial force with magnitude

$$f_{\mathrm{pr}} = \left(\frac{L}{4\pi r^2 c}\right)\pi a^2 Q_{\mathrm{pr}}. \tag{24}$$

If the dust grain has internal density ρ_{gr}, we can also express the radial force in terms of the grain mass m and radial velocity v_r as

$$f_{\mathrm{pr}} = m\frac{\mathrm{d}v_r}{\mathrm{d}t} = \frac{4\pi}{3}\rho_{\mathrm{gr}}a^3 v_r \frac{\mathrm{d}v_r}{\mathrm{d}r}, \tag{25}$$

where in this problem we neglect the drag force and other external forces. Equating these two expressions,

$$2v_r\,\mathrm{d}v_r = \left(\frac{3LQ_{\mathrm{pr}}}{8\pi c\rho_{\mathrm{gr}}a}\right)\left(\frac{\mathrm{d}r}{r^2}\right). \tag{26}$$
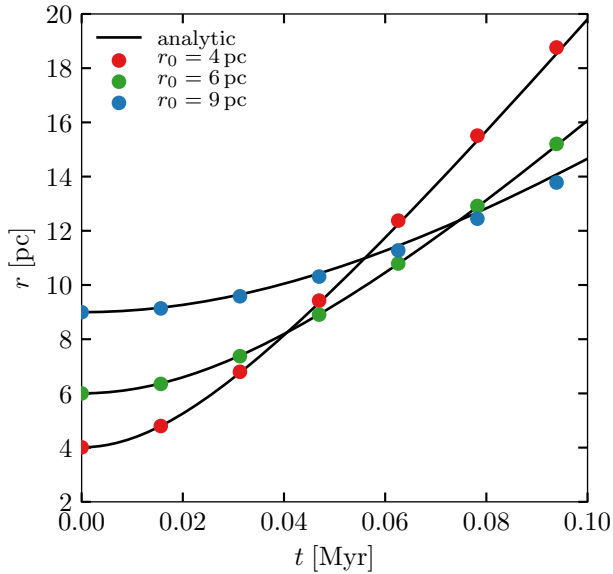
Figure 2. Radial distance versus time for a sample of dust grains moving away from a source of constant luminosity. Simulation results are shown in colour, while analytic predictions are in black. Grains have fixed size but different values of r_0, the initial radial distance from the radiation source. In this test, we neglect drag between dust and gas and include only radiation pressure on dust.

Figure 3. Number of photons N remaining as a function of time for a test in which a burst of radiation is incident on a thin layer of dust. We normalize by the initial number of photons N_0. Coloured lines show simulation results at different resolutions, with the labels indicating number of gas cells. The dotted line shows the expected analytic behaviour, with the photon fraction dropping as it passes through the dust layer.

Integrating for a dust grain starting at rest at $r = r_0$, one obtains a relation between dust grain radial velocity and radial distance,

$$v_r = \frac{dr}{dt} = \sqrt{\frac{3LQ_{pr}}{8\pi c \rho_{gr} a}\left(\frac{1}{r_0} - \frac{1}{r}\right)}. \qquad (27)$$

As $r \to \infty$, the dust grain approaches a constant terminal velocity. Grains starting at smaller initial radii, closer to the radiation source, have larger terminal velocities.

We place a monochromatic source of luminosity $L = 10^6\,L_\odot$ at the center of a three-dimensional box of side length $160\,\text{pc}$. The volume is tessellated by 256^3 gas cells with uniform density $n = 1\,\text{cm}^{-3}$. The positions of mesh-generating points are initially arranged on an equispaced Cartesian lattice. Then, points are uniformly randomly displaced in each dimension by up to 20 per cent of the initial cell size in order to produce an irregular mesh. This approximates the cell geometries seen in typical simulations (Vogelsberger et al. 2012; Kannan et al. 2019b). To model the luminosity source, during every time-step photons are injected in equal amounts into gas cells within $1\,\text{pc}$ of the box center. For completeness, we assume photons have energy $13.6\,\text{keV}$, though this choice does not affect our results.

We place 256^3 dust particles on an equispaced Cartesian lattice. Dust particles are given equal mass to model an initially uniform dust distribution. The dust particle mass is chosen so that the total dust-to-gas ratio is 0.5. However, to focus solely on the effect of radiation pressure, in this test we neglect any drag coupling between dust and gas. As a result, the value of the dust-to-gas ratio does not affect results. We also assume that only dust particles provide opacity to radiation: the opacity of gas cells is set to zero, and we turn off gas thermochemistry so that the gas begins and remains purely neutral hydrogen. Thus, the gas is analytically expected to remain at rest.

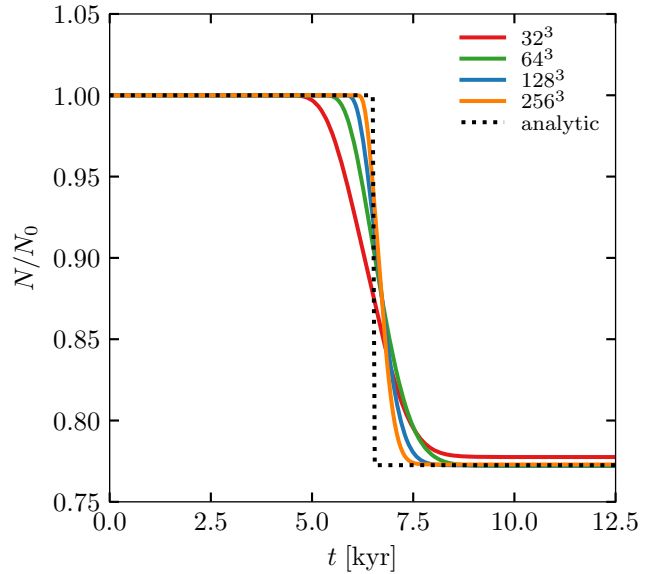Dust particles are assumed to have grains of size $a = 0.01\,\mu\text{m}$

and internal density $\rho_{gr} = 2.4\,\text{g}\,\text{cm}^{-3}$. For simplicity, we assume that a grain's radiation pressure cross section equals its geometric cross section and set $Q_{pr} = 1$. When calculating radiation transport, we adopt the reduced speed of light approximation (in the notation of Kannan et al. 2019b, we set $\tilde{c}/c = 1/25$). This reduces the rate at which photons cross the simulation domain and in turn lessens noise in photon fluxes near the box edges where photons meet.

Figure 2 shows the time evolution of a sample of dust particles as they move away from the radiation source. We select dust particles that begin at initial radial distances of $r_0 = 4, 6,$ and $9\,\text{pc}$. We compare the radial motion of these simulation particles over a time period of $0.1\,\text{Myr}$ with the expected behaviour obtained by numerically integrating equation (27). The initial radiation force is greater for dust grains closer to the luminosity source. As a result, by $t = 0.1\,\text{Myr}$ the grain initially closest to the luminosity source ($r_0 = 4\,\text{pc}$) develops the largest velocity and is at the furthest radial distance. In contrast, the grain starting at $r_0 = 9\,\text{pc}$ lags behind those two starting closer to the source. While radiation pressure does drive the dust outwards, the resulting distribution does not preserve the initial ordering of grains in terms of radial distance from the luminosity source.

The simulation results largely agree with the expected behaviour. There are some minor deviations above (e.g. $r_0 = 4\,\text{pc}$) and below (e.g. $r_0 = 9\,\text{pc}$) the analytic solutions, likely influenced by the fact that we update dust particle positions using kernel-interpolated estimates of the gas cell radiation flux. However, we have verified that these deviations diminish as the resolution of the test problem increases. Figure 2 demonstrates the suitability of our hybrid gas cell and dust particle approach for modelling radiation pressure on dust grains.
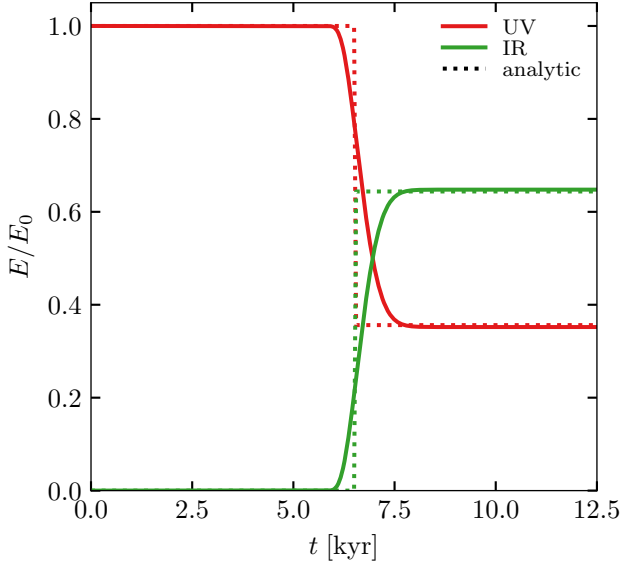
Figure 4. Fraction of energy in UV (red) and IR (green) photons in a test where UV radiation is incident on a thin layer of dust. Dust grains absorb UV photons and reemit in the IR, and we turn off absorption of IR photons so that the total energy in radiation is constant. Dotted lines show the expected analytic result, given the optical depth $\tau \approx 1$.
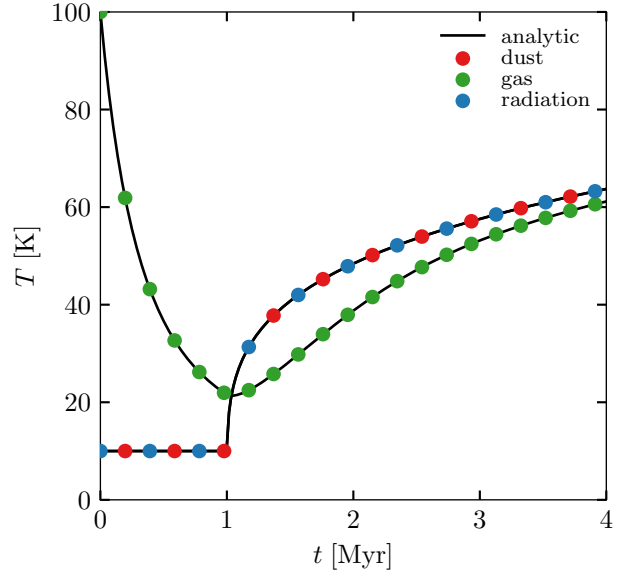

Figure 5. Temperature evolution for a test in which dust (red) is coupled to gas (green) through collisional energy exchange and to IR radiation (blue) through thermal IR emission and absorption. The test includes injecting IR photons into every gas cell at a constant rate starting at $t = 1$ Myr to mimic a radiation source. Coloured points show simulation results, while black lines indicate the expected solution by numerically integrating the analytic energy exchange equations. Dust and radiation temperatures are highly coupled, while the gas temperature is slower to change.

3.3 Photon absorption by dust grains

We demonstrate the ability of dust grains to absorb photons in our hybrid dust particle and gas cell scheme using a simplified test problem, where radiation is incident on a thin layer of dust.

We begin with a lattice of N^3 equispaced gas cells of uniform density $n = 1\,\mathrm{cm}^{-3}$ in a box of side length $L = 160\,\mathrm{pc}$. Cell centers are uniformly randomly displaced by up to 20 per cent in each coordinate, except for the two leftmost and two rightmost layers of cells along the x axis, where the mesh remains Cartesian. A layer of N^2 equispaced, equal-mass dust particles is placed halfway through the box at $x = L/2$, with the dust particle mass m_d chosen so that the total dust-to-gas ratio is 10^{-3}. Both dust and gas components start at rest, and in this test of radiation dynamics we switch off self-gravity and the drag force. Dust particles are assumed to consist entirely of $a = 0.01\,\mu$m sized grains of density $\rho_\mathrm{gr} = 2.4\,\mathrm{g\,cm}^{-3}$, and we take $Q_\mathrm{abs} = 1$. This simplifies the expected analytic behaviour, but in principle dust particles could be populated with a full distribution of grain sizes.

For the initial conditions, we place radiation of uniform energy density in the N^2 gas cells bordering the $x = 0$ edge of the box. The radiation flux points in the positive x direction and has its maximally allowed magnitude (following the notation of Kannan et al. 2019b, $|\mathbf{F_r}| = \tilde{c}E_r$). We use reduced speed of light $\tilde{c} = c/25$ for photon propagation. In this test, we use one UV bin and switch off hydrogen and helium thermochemistry so that dust grains provide the only source of opacity. Dust particles spread their opacity over the $N_\mathrm{ngb} = 64$ neighboring gas cells, though our results are largely insensitive to this choice.

Figure 3 shows the number fraction of photons remaining in the box as a function of time, for four resolution tests ($N = 32, 64, 128,$ and 256). Analytically, the photons reach the layer of dust at $x = L/2$ in time $t = L/(2\tilde{c}) \approx 6.5\,\mathrm{kyr}$, after which the number fraction should drop from 1 to $\exp(-\tau)$, in terms of the

optical depth

$$\tau = \int_0^L n(x)\,\sigma\;\mathrm{d}x \qquad (28)$$

where $n(x) = \delta(x - L/2) \times N^2/L^2$ is the number density of dust particles and $\sigma = (3m_\mathrm{d})/(4\rho_\mathrm{gr}a)$ is the total cross section of each dust particle. For our choice of parameters above, $\tau \approx 0.26$. There is strong agreement between the analytic prediction and simulation results, with the late-time photon number fraction dropping to $\exp(-\tau)$ as expected. Increasing the resolution of the test produces a sharper drop in photon number fraction, since the gas cells surrounding the dust layer have smaller extent.

3.4 Dust reprocessing

To demonstrate the ability for dust grains to absorb UV photons and reemit in the IR, we extend the test presented in Figure 3, where UV photons incident upon a thin dust layer were strictly absorbed and not reemitted. In this new test, we adopt one UV and one IR radiation bin and convert absorbed UV energy to IR energy. We neglect dust grain emission and absorption in the IR, so that the total energy in radiation is constant and simply shifts between frequency bins.

The initial conditions are the same as in Figure 3, except that we decrease the fixed grain size to $a = 2.5 \times 10^{-3}\,\mu$m. Since the dust particle mass is unchanged, the cross section per dust particle increases by a factor of four, and the optical depth through the dust layer is $\tau \approx 1$. We pick a resolution of $N = 128$ for gas cells and dust particles.

Figure 4 shows the fraction of radiation energy in UV and IR bins as a function of time, along with the expected analytic be-
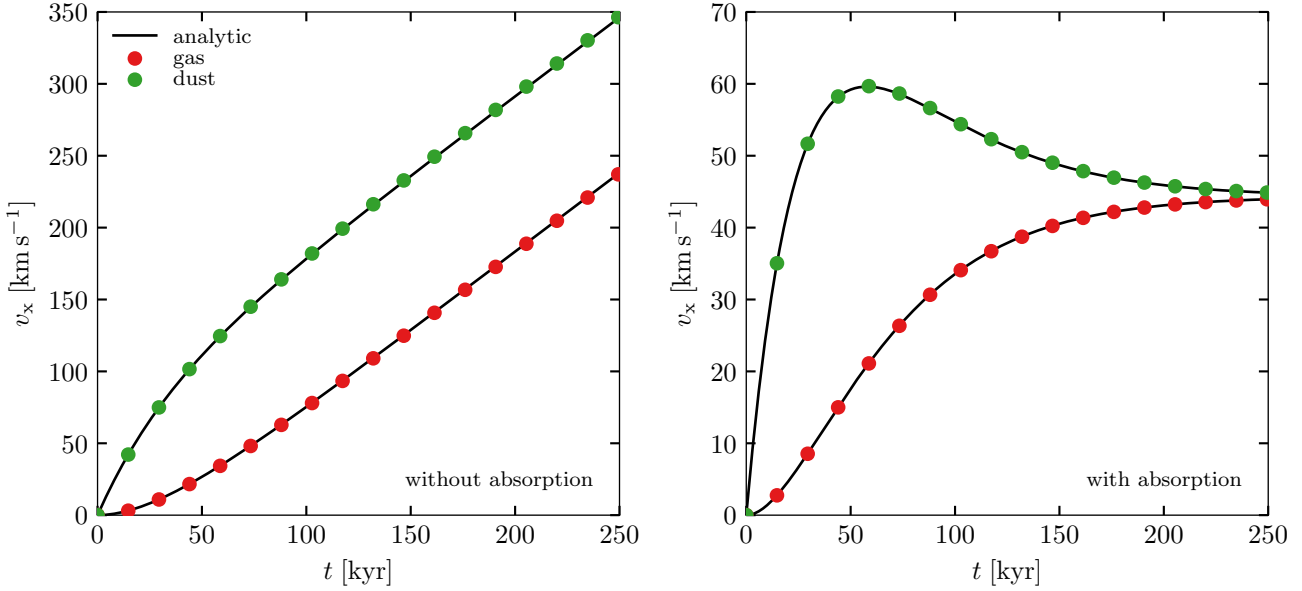
Figure 6. Left panel: mean velocity of gas (red) and dust (green) versus time for a test in which dust grains feel radiation pressure but do not absorb photons so that the radiation flux is constant. Analytic profiles are shown in black. Radiation accelerates dust, which in turn drags gas. The rate of momentum injection from radiation remains constant. Right panel: similar results for a test with photon absorption included. As the photon flux drops, dust and gas velocities equilibrate through drag. In both panels, simulation output is subsampled to improve readability.

haviour. The optical depth $\tau \approx 1$ is chosen in this test so that a majority of UV energy converts to IR as photons pass through the dust layer. We note that, since IR photons are lower energy than UV photons, this test implies an increase in the total number of photons. Our results agree with the analytic prediction that the fraction of energy in UV and IR bins reaches $e^{-\tau}$ and $1 - e^{-\tau}$, respectively.

3.5 Thermal coupling

We next present a test in which dust, gas, and radiation are thermally coupled through the system in equation (18). In a box of side length 1 kpc, we place an irregular mesh of 32^3 gas cells with uniform density $n = 1\,\text{cm}^{-3}$ and an equispaced lattice of 32^3 dust particles. We set the dust-to-gas ratio $D = 1$, fixed grain size $a = 0.005\,\mu\text{m}$ (i.e. here, we do not place grains in multiple size bins), efficiencies $Q_{\text{abs}} = 1$, and internal grain density $\rho_{\text{gr}} = 2.4\,\text{g cm}^{-3}$. Dust and gas components initially start at rest, although we do not focus on dynamics in this test.

The initial dust and gas temperatures are $T_{\text{d}} = 10\,\text{K}$ and $T_{\text{g}} = 100\,\text{K}$, respectively, and we choose the initial IR radiation density so that the radiation temperature $T_{\text{r}} \equiv (E_{\text{IR}}/a_{\text{B}})^{1/4} = 10\,\text{K}$ at the start. We do not use a reduced speed of light, so that $\tilde{c} = c$. To mimic a radiation source that emits in the IR, starting at $t = 1\,\text{Myr}$ we inject IR photons into gas cells at the constant rate $\dot{E}_{\text{IR}} = 1.2 \times 10^{57}\,\text{erg Myr}^{-1}\,\text{kpc}^{-3}$. In this setup, we set radiation in non-IR bins to zero and do not include other sources of gas thermal change (e.g. from photoheating) beyond dust-gas collisional energy exchange.

Figure 5 shows the evolution of dust, gas, and radiation temperatures, computed by averaging over simulation gas cells and dust particles. Since the gas temperature initially is greater than the dust temperature, the gas begins to collisionally cool. Because of the strong dependence of dust-radiation energy exchange on dust temperature, the dust temperature does not significantly change as

the gas temperature drops. When the IR radiation injection begins at $t = 1\,\text{Myr}$, dust remains highly coupled with radiation. In contrast, the gas temperature lags behind the increase in dust and radiation temperatures. Our simulation results closely follow the predictions obtained by integrating the analytic system in equation (18), where we adopt the silicate grain heat capacity from Dwek (1986) to relate dust internal energy change to dust temperature change. This test shows how dust, gas, and radiation temperatures can evolve according to energy exchange processes and external sources.

3.6 Coevolution of radiation, dust, and gas through radiation pressure and drag

Previous tests illustrated the effect of drag without radiation (e.g. Figure 1) or radiation without drag (e.g. Figures 2, 3, 4, and 5). We now demonstrate the ability of our methods to simultaneously handle drag and radiation.

The initial conditions consist of uniform dust and gas distributions at rest and are identical to those used in Section 2.1.4, except that we set the dust-to-gas ratio $D = 0.5$ and fixed grain size $a = 0.1\,\mu\text{m}$. We initialise a uniform monochromatic radiation field whose flux has magnitude $F_0 = 10\,\text{erg s}^{-1}\,\text{cm}^{-2}$ pointing in the $\hat{x}$ direction. Dust particles contribute the only opacity to radiation (i.e. we neglect gas thermochemistry and opacity contributed by gas cells), and photons propagate at the reduced speed of light $\tilde{c} = c/1000$. As a result, in this test dust grains accelerate from photon radiation pressure and in turn accelerate the gas through drag. In addition to our fiducial setup where dust grains both feel radiation pressure and absorb photons, we also perform a test where photon absorption is turned off so that analytically the radiation flux $\mathbf{F}(t) = F_0\hat{x}$ at all times.

To ensure our simulation results can be compared with analytic predictions, we require that the stopping time-scale t_{s} is con-

stant. For this test only, we disable the injection of thermal energy into the gas from drag dissipation of kinetic energy. Thus, the sound speed is expected to remain constant. Additionally, in equation (3) we neglect the correction term in parentheses. In Appendix A, we show how to analytically integrate the dust and gas equations of motion.

The choice of parameters above yield a stopping time-scale t_s and photon decay time-scale t_d both on the order of $40\,\mathrm{kyr}$. If we had $t_s \ll t_d$, radiation pressure would essentially move dust and gas together as one, while $t_s \gg t_d$ would see photons rapidly deposit momentum into dust and decay away before drag accelerated gas. In our setup, dust, gas, and radiation coevolve over similar time-scales.

Figure 6 shows the mean velocity of gas cells and dust particles as a function of time. In addition to the fiducial setup with $t_s \approx t_d$, we also perform a test neglecting photon absorption by dust grains. In this test, which is equivalent to taking $t_d \to \infty$, radiation flux remains constant and continually imparts momentum to the dust at a fixed rate. Runs with and without photon absorption show different qualitative evolution, though in both cases simulation results closely follow analytic results.

Without absorption, dust and gas velocities increase in time without bound. Initially, dust accelerates more quickly than gas, since only dust feels radiation pressure. At later times, dust and gas feel roughly the same acceleration, with the velocity offset $v_d - v_g \approx 108\,\mathrm{km\,s^{-1}}$ matching the analytic prediction of $F_0 \kappa t_s/c$.

With absorption, dust still feels a larger initial acceleration. However, as photons get absorbed, the rate of momentum injection decays to zero and dust and gas velocities equilibrate via the drag force. Thus, there is no long-term velocity offset between dust and gas components. The steady-state velocities $v_d \approx v_g \approx 44\,\mathrm{km\,s^{-1}}$ agree with the analytic expectation of $F_0 \kappa D t_d/[(1 + D)c]$.

4 CONCLUSIONS

We have developed a framework to couple dust physics and radiation hydrodynamics in the moving-mesh code AREPO-RT, where dust is modelled using live simulation particles and radiation is handled on an unstructured mesh. We first extend our implementation of the aerodynamic drag force that couples dust and gas motion to properly capture dynamics at arbitrary dust-to-gas ratios, even those well above Galactic values. We then describe kernel-smoothed methods to model the interaction between dust and radiation, where grain cross sections from simulation dust particles are interpolated onto neighboring gas cells to affect radiation fields in a self-consistent manner.

We detail our approach for calculating radiation pressure forces on populations of dust grains, including those covering a range of different grain sizes. This method is tested using a constant luminosity source in a medium with an initially uniform dust density, for which analytic behaviour is known. We model absorption of photons by local dust grains and maintain the ability of AREPO-RT to treat multifrequency radiation, where UV and optical photons are single-scattered and IR photons are multi-scattered. We illustrate the ability for dust to absorb photons passing through a thin layer of dust of known optical depth. Instead of assuming dust and gas are in local thermodynamic equilibrium, we allow dust and gas to have separate temperatures and model their energy exchange through collisional processes. Dust and radiation also exchange energy through absorption and thermal dust emission at IR wavelengths.

Finally, we demonstrate the evolution of a mixture of dust, gas, and radiation using our hybrid dust particle and gas cell scheme. Dust and gas are coupled through aerodynamic drag, and dust and radiation are coupled through radiation pressure and photon absorption. In agreement with analytic predictions, we verify that dust and gas velocities initially deviate as photons accelerate dust but later equilibrate through drag as all photons get absorbed. This behaviour more closely mirrors the expected physics compared to models that assume a perfect coupling between dust and gas.

We emphasise the original nature of our methods in comparison to typical radiation hydrodynamics schemes that model dust opacity using fixed values or simplified functions of hydrodynamic quantities like temperature. By treating dust using live simulation particles subject to dynamical forces, our approach avoids the need to make assumptions about the local dust-to-gas ratio and dust distribution and instead calculates dust opacity self-consistently based on the local grain abundance. While there are codes to perform radiative transfer in arbitrary dusty media, these usually run in post-processing and not concurrently with hydrodynamic evolution. As radiation hydrodynamic simulations of galaxy formation become more computationally tractable, our model for the interaction of dust and radiation is an alternative to simulations that neglect a direct treatment of dust.

REFERENCES

Abel T., Norman M. L., Madau P., 1999, ApJ, 523, 66
Abel T., Wandelt B. D., 2002, MNRAS, 330, L53
Agertz O., Kravtsov A. V., 2015, ApJ, 804, 18
Agertz O., Kravtsov A. V., Leitner S. N., Gnedin N. Y., 2013, ApJ, 770, 25
Aumer M., White S. D. M., Naab T., Scannapieco C., 2013, MNRAS, 434, 3142
Barnes D. J., Kannan R., Vogelsberger M., Marinacci F., 2018, arXiv e-prints, arXiv:1812.01611
Bernstein R. A., Freedman W. L., Madore B. F., 2002, ApJ, 571, 56
Bieri R., Dubois Y., Rosdahl J., Wagner A., Silk J., Mamon G. A., 2017, MNRAS, 464, 1854
Bjorkman J. E., Wood K., 2001, ApJ, 554, 615
Boulanger F., Perault M., 1988, ApJ, 330, 964
Burke J. R., Hollenbach D. J., 1983, ApJ, 265, 223
Camps P., Baes M., 2015, Astronomy and Computing, 9, 20
Camps P. et al., 2015, A&A, 580, A87
Costa T., Rosdahl J., Sijacki D., Haehnelt M. G., 2018a, MNRAS, 473, 4197
Costa T., Rosdahl J., Sijacki D., Haehnelt M. G., 2018b, MNRAS, 479, 2079

Dale D. A., Helou G., Contursi A., Silbermann N. A., Kolhatkar S., 2001, ApJ, 549, 215

Draine B. T. et al., 2007, ApJ, 663, 866

Draine B. T., Lee H. M., 1984, ApJ, 285, 89

Draine B. T., Li A., 2001, ApJ, 551, 807

Dubroca B., Feugeas J., 1999, Academie des Sciences Paris Comptes Rendus Serie Sciences Mathematiques, 329, 915

Dwek E., 1986, ApJ, 302, 363

Ferrara A., Ferrini F., Barsella B., Franco J., 1991, ApJ, 381, 137

Goldsmith P. F., 2001, ApJ, 557, 736

González M., Audit E., Huynh P., 2007, A&A, 464, 429

Greif T. H., 2014, MNRAS, 444, 1566

Guhathakurta P., Draine B. T., 1989, ApJ, 345, 230

Hollenbach D., McKee C. F., 1979, ApJS, 41, 555

Hollenbach D., McKee C. F., 1989, ApJ, 342, 306

Hopkins P. F., Grudić M. Y., 2019, MNRAS, 483, 4187

Hopkins P. F., Kereš D., Oñorbe J., Faucher-Giguère C.-A., Quataert E., Murray N., Bullock J. S., 2014, MNRAS, 445, 581

Hopkins P. F., Quataert E., Murray N., 2011, MNRAS, 417, 950

Hopkins P. F., Quataert E., Murray N., 2012, MNRAS, 421, 3522

Jaura O., Glover S. C. O., Klessen R. S., Paardekooper J.-P., 2018, MNRAS, 475, 2822

Kannan R., Marinacci F., Vogelsberger M., Sales L. V., Torrey P., Springel V., Hernquist L., 2019a, arXiv e-prints, arXiv:1910.14041

Kannan R., Vogelsberger M., Marinacci F., McKinnon R., Pakmor R., Springel V., 2019b, MNRAS, 485, 117

Krumholz M. R., 2014, MNRAS, 437, 1662

Krumholz M. R., 2018, MNRAS, 480, 3468

Krumholz M. R., Matzner C. D., 2009, ApJ, 703, 1352

Krumholz M. R., Thompson T. A., 2013, MNRAS, 434, 2329

Laibe G., Price D. J., 2012, MNRAS, 420, 2345

Laor A., Draine B. T., 1993, ApJ, 402, 441

Levermore C. D., 1984, Journal of Quantitative Spectroscopy and Radiative Transfer, 31, 149

Lorén-Aguilar P., Bate M. R., 2015, MNRAS, 454, 4114

McKinnon R., Torrey P., Vogelsberger M., 2016, MNRAS, 457, 3775

McKinnon R., Vogelsberger M., Torrey P., Marinacci F., Kannan R., 2018, MNRAS, 478, 2851

Murray N., Quataert E., Thompson T. A., 2005, ApJ, 618, 569

Murray N., Quataert E., Thompson T. A., 2010, ApJ, 709, 191

Omukai K., 2000, ApJ, 534, 809

Oxley S., Woolfson M. M., 2003, MNRAS, 343, 900

Paardekooper S.-J., Mellema G., 2006, A&A, 453, 1129

Pavlyuchenkov Y. N., Wiebe D. S., Akimkin V. V., Khramtsova M. S., Henning T., 2012, MNRAS, 421, 2430

Popescu C. C., Tuffs R. J., 2002, MNRAS, 335, L41

Price D. J. et al., 2017, arXiv:1702.03930

Reissl S., Klessen R. S., Mac Low M.-M., Pellegrini E. W., 2018, A&A, 611, A70

Rosdahl J., Blaizot J., Aubert D., Stranex T., Teyssier R., 2013, MNRAS, 436, 2188

Rosdahl J. et al., 2018, MNRAS, 479, 994

Rosdahl J., Schaye J., Teyssier R., Agertz O., 2015, MNRAS, 451, 34

Rosdahl J., Teyssier R., 2015, MNRAS, 449, 4380

Roškar R., Teyssier R., Agertz O., Wetzstein M., Moore B., 2014, MNRAS, 444, 2837

Schlafly E. F., Finkbeiner D. P., 2011, ApJ, 737, 103

Schlegel D. J., Finkbeiner D. P., Davis M., 1998, ApJ, 500, 525

Siebenmorgen R., Kruegel E., Mathis J. S., 1992, A&A, 266, 501

Silva L., Granato G. L., Bressan A., Danese L., 1998, ApJ, 509, 103

Smith A., Ma X., Bromm V., Finkelstein S. L., Hopkins P. F., Faucher-Giguère C.-A., Kereš D., 2019, MNRAS, 484, 39

Smith B. D. et al., 2017, MNRAS, 466, 2217

Soifer B. T., Neugebauer G., 1991, AJ, 101, 354

Springel V., 2010, MNRAS, 401, 791

Thompson T. A., Fabian A. C., Quataert E., Murray N., 2015, MNRAS, 449, 147

Tsang B. T.-H., Milosavljević M., 2015, MNRAS, 453, 1108

Vogelsberger M., Sijacki D., Kereš D., Springel V., Hernquist L., 2012, MNRAS, 425, 3024

Weingartner J. C., Draine B. T., 2001, ApJ, 553, 581

Wise J. H., Abel T., Turk M. J., Norman M. L., Smith B. D., 2012, MNRAS, 427, 311

Woitke P., 2006, A&A, 452, 537

Wu X., Kannan R., Marinacci F., Vogelsberger M., Hernquist L., 2019a, MNRAS, 488, 419

Wu X., McQuinn M., Kannan R., D'Aloisio A., Bird S., Marinacci F., Davé R., Hernquist L., 2019b, MNRAS, 2405

APPENDIX A: ANALYTIC SOLUTION FOR RADIATION, DUST, AND GAS COEVOLUTION TEST PROBLEM

We consider the analytic evolution of the dust and gas mixture described in Section 3.6 according to drag and radiation pressure.

By symmetry, the x components of the dust and gas velocities, v_d and v_g respectively, are independent of position and dependent only on time. They evolve according to

$$\frac{dv_d}{dt} = -\frac{v_d(t) - v_g(t)}{t_s(1+D)} + \frac{F(t)\kappa}{c} \tag{A1}$$

and

$$\frac{dv_g}{dt} = D\frac{v_d(t) - v_g(t)}{t_s(1+D)}, \tag{A2}$$

where $F(t)$ is the radiation flux in the $\hat{x}$ direction, $D = \rho_d/\rho_g$ is the dust-to-gas ratio, t_s is the drag stopping time-scale and c is the speed of light. Here, the grain opacity $\kappa = (3Q_{abs})/(4\rho_{gr}a)$ for grain size a and grain density ρ_{gr} is the absorption cross section *per unit dust mass*. Additionally, the gas remains at uniform density and internal energy and feels no pressure gradient.

To solve these equations analytically, we first define the state vector

$$\mathbf{w}(t) = \begin{pmatrix} v_d(t) \\ v_g(t) \end{pmatrix}, \tag{A3}$$

and the matrix

$$\mathbf{A} = \frac{1}{t_s(1+D)}\begin{pmatrix} -1 & 1 \\ D & -D \end{pmatrix}. \tag{A4}$$

Matrix $\mathbf{A}$ has eigenvalues $\lambda_1 = -1/t_s$ and $\lambda_2 = 0$, with corresponding eigenvectors $\mathbf{x_1} = (-1/D, 1)^T$ and $\mathbf{x_2} = (1, 1)^T$, respectively. We introduce the inhomogeneous source vector

$$\mathbf{f}(t) = \begin{pmatrix} F(t)\kappa/c \\ 0 \end{pmatrix}. \tag{A5}$$

Over elapsed time t, photons experience an optical depth of $\tau(t) = \rho_d\kappa\tilde{c}t$, where $\tilde{c}$ is the (possibly reduced) speed of photon propagation. This gives a uniform radiation flux at time t of $F(t) = $

$F_0 \exp(-\tau(t)) = F_0 \exp(-t/t_d)$, written in terms of decay time-scale $t_d \equiv 1/(\rho_d \kappa \tilde{c})$. The coupled equations (A1) and (A2) can be written in vector form as

$$\frac{\mathrm{d}\mathbf{w}}{\mathrm{d}t} = \mathbf{A}\mathbf{w}(t) + \mathbf{f}(t). \tag{A6}$$

Since gas and dust start at rest, the initial condition is $\mathbf{w}(0) = (0,0)^{\mathrm{T}}$.

We define the helper matrix

$$\mathbf{X}(t) = \begin{pmatrix} \mathbf{x_1}e^{\lambda_1 t} & \mathbf{x_2}e^{\lambda_2 t} \end{pmatrix} = \begin{pmatrix} -\frac{1}{D}e^{-t/t_s} & 1 \\ e^{-t/t_s} & 1 \end{pmatrix}, \tag{A7}$$

whose inverse is given by

$$\mathbf{X}^{-1}(t) = \frac{1}{1+D}\begin{pmatrix} -De^{t/t_s} & De^{t/t_s} \\ D & 1 \end{pmatrix}. \tag{A8}$$

Then, the general solution to equation (A6) is

$$\mathbf{w}(t) = C_1 \begin{pmatrix} -1/D \\ 1 \end{pmatrix} e^{-t/t_s} + C_2 \begin{pmatrix} 1 \\ 1 \end{pmatrix} + \mathbf{w_P}(t) \tag{A9}$$

where C_1 and C_2 are constants necessary to match the initial condition and

$$\mathbf{w_P}(t) = \mathbf{X}(t) \int \mathbf{X}^{-1}(t)\mathbf{f}(t) \, \mathrm{d}t \tag{A10}$$

is the particular solution. Since the only time dependence in equation (A10) is exponential, the particular solution can be directly computed. For brevity, we omit the form of $\mathbf{w_P}(t)$ and constants C_1 and C_2.

By defining the time-scale t_* via

$$\frac{1}{t_*} \equiv \frac{1}{t_s} - \frac{1}{t_d}, \tag{A11}$$

we can write the analytic velocity evolution for dust as

$$v_d(t) = \frac{F_0 \kappa}{(1+D)c}\left[-t_* e^{-t/t_s} + Dt_d \right.$$
$$\left. + t_* e^{-t/t_d} - Dt_d e^{-t/t_d} \right] \tag{A12}$$

and for gas as

$$v_g(t) = \frac{DF_0 \kappa}{(1+D)c}\left[t_* e^{-t/t_s} + t_d \right.$$
$$\left. - t_* e^{-t/t_d} - t_d e^{-t/t_d} \right]. \tag{A13}$$

Analytic profiles for the case where dust grains feel radiation pressure but do not absorb photons (i.e. substituting $F(t) = F_0$ in equation A5) can be obtained by taking the limit as the photon decay time-scale $t_d \to \infty$.